

First-principles study of metal-induced gap states in metal/oxide interfaces and their relation with the complex band structure

Pablo Aguado-Puente¹ and Javier Junquera¹

¹*Departamento de Ciencias de la Tierra y Física de la Materia Condensada,
Universidad de Cantabria, Cantabria Campus Internacional,
Avenida de los Castros s/n, 39005 Santander, Spain*

(Dated: January 13, 2014)

We develop a simple model to compute the energy-dependent decay factors of metal-induced gap states in metal/insulator interfaces considering the collective behaviour of all the bulk complex bands in the gap of the insulator. The agreement between the penetration length obtained from the model (considering only bulk properties) and full first-principles simulations of the interface (including explicitly the interfaces) is good. The influence of the electrodes and the polarization of the insulator is analyzed. The method simplifies the process of screening materials to be used in Schottky barriers or in the design of giant tunneling electroresistance and magnetoresistance devices.

PACS numbers: 73.40.Gk, 73.30.+y, 77.80.Fm, 31.15.A-

Interfaces between different oxide materials exhibit a fantastic variety of functional properties, some of them intrinsic to the boundary between the constituent compounds [1]. A ubiquitous type of interface is that formed between a metal and an insulator or semiconductor, since the presence of electrodes is required for the application of electric fields in solid state devices. At any metal/insulator interface, bulk Bloch states in the metal side of the junction with eigenvalues below the Fermi energy and within the energy gap of the insulator cannot propagate into the insulating side. These states do not vanish right at the interface either, but they decay exponentially as they penetrate into the insulator [2]. Indeed, the tails of the metal Bloch states might have a significant amplitude for a few layers from the interface, creating a continuum of gap states [the so-called metal-induced gap states (MIGS)] [2]. These MIGS are essential to determine many interfacial properties. The transfer of charge associated to them contribute to the interfacial dipole, which enter into most of the models describing the formation of Schottky barriers. For this reason, theory of MIGS were deeply studied in semiconductor heterostructures [3, 4]. More recently, the attention has turned to metal/oxide interfaces, mostly due to several works that have first predicted [5, 6] and later demonstrated giant tunnel electroresistance [7–10] and magnetoresistance [11–13] in ferroelectric/metal junctions, where the decay length of the MIGS plays a major role.

The eigenstates of the Hamiltonian for the interface can be described as the matching at the junction of two wave functions: an ordinary bulk Bloch state on the metal side, and an exponentially decaying function on the insulator side. Assuming that the interface is periodic in the plane parallel to the boundary [referred to as the (x, y) plane], then the components of the wave vectors parallel to the interface, \mathbf{k}_{\parallel} , are real and have to be preserved when the electron crosses the junction [14].

Therefore, the previous matching is possible only if the two wave functions do have the same associated energy, symmetry, and \mathbf{k}_{\parallel} [15].

The exponential tails within the insulator decay only in the direction perpendicular to the junction (referred to as the z -direction), and can be actually regarded as Bloch functions of the bulk insulator with an associated *complex* wave vector in the perpendicular direction $k_{\perp} = k_z + iq$ [14]. The decay length of the wave function is given by $1/q$. For this reason, despite being a genuine interface property, characteristics of MIGS are often discussed in terms of the *complex band structure* (CBS) of the bulk insulating material [2]. This analysis is useful because it allows to predict the characteristics of MIGS and other interface properties from the simulation of a bulk material, avoiding the much more computationally demanding simulation of a realistic interface. Accordingly, many studies have taken advantage of the relatively straightforward interpretation provided by the CBS to shed light into interface phenomena such as tunneling magnetoresistance [11], or the confinement of two-dimensional electron gases [16], with the discussion often focused on complex bands at high symmetry points of the Brillouin zone [17].

Despite the previous efforts, a direct comparison of the spatial and energetic distribution of the evanescent states coming from the CBS (i.e. considering only bulk properties), with the MIGS obtained in a realistic simulation of the interface (i.e. taking into account atomic details at the junction) are only available in simple molecular electronic systems [18]. Up to our knowledge, this study is absolutely absent in complex oxide interfaces, where extra degrees of freedom such as the spontaneous polarization in the insulator might alter and tune their properties. Here, we analyze the bulk CBS of an insulator (PbTiO_3) and give a recipe to estimate the decay factor of the MIGS from the collective contributions of all the

complex bands. We show, contrary to earlier assumptions, that the analysis of the full Brillouin zone (and not only the high-symmetry points) is necessary to accurately estimate the effective decay factor of the MIGS in the insulating layer. We further demonstrate the validity of such approach by comparing with decay factors obtained from explicit simulations of realistic capacitors. The agreement between the penetration length estimated from the CBS and the one observed after simulations of realistic capacitors is very good, especially remarkable when a noble metal (Pt) is used as electrode. When the electrode is replaced by a metal oxide (SrRuO₃), the dependency of the decay factor with the energy shows some extra structure due to interfacial effects (symmetry filtering). In thin film capacitors with SrRuO₃ electrodes, where the polarization of the PbTiO₃ layer is smaller than the bulk spontaneous value due to imperfect screening, ferroelectricity does not modify strongly the penetration length. Larger values of the polarization produce a decrease of the penetration of the MIGS.

We have carried out simulations within the local density approximation as implemented in two different codes: SIESTA [19] for the calculations of realistic interfaces, and QUANTUM-ESPRESSO [20] for the CBS computations of bulk materials [21]. The details of the simulations can be found in the supplemental data.

Complex band structure of bulk PbTiO₃. In order to face the difficulty of the problem step by step, we have proceed first with a centrosymmetric tetragonal phase (*P4/mmm* space group), assuming the in-plane theoretical lattice constant, a , of an hypothetically thick SrTiO₃ substrate and only allowing the out-of-plane lattice constant, c , to relax. This is the structure that PbTiO₃ displays at the center of the unpolarized capacitor.

In essence a CBS calculation consists in sampling the two-dimensional Brillouin zone (2DBZ) parallel to the interface, and for every \mathbf{k}_{\parallel} search for complex k_{\perp} associated with real eigenvalues of the system. Imaginary bands always connect extrema of other bands (either real or complex) [22], and it is often assumed that complex bands with the shortest imaginary wave vector q are those connecting the edges of the valence and conduction bands. The analysis of the real band structure (see Suppl. Fig. 2 in supplemental data) reveals that, in the non polar *P4/mmm* phase, PbTiO₃ possesses a direct gap at X, $(\pi/a, 0, 0)$, and a slightly larger one at Z, $(0, 0, \pi/c)$.

Complex bands at such high symmetry points have an associated \mathbf{k} with the form $(\pi/a, 0, iq)$ and $(0, 0, \pi/c + iq)$ respectively, which correspond to complex bands at $\mathbf{k}_{\parallel} = \bar{X}$ and $\bar{\Gamma}$ in the 2DBZ, shown in Fig. 1(a) and (b). We observe that the states with the shortest q (largest penetration lengths) consist of a Δ_1 singlet in the lower energy part of the band gap and a Δ_5 doublet for energies close to the conduction band edge. The smaller decay factor q takes values from 0.10 to 0.15 in units of $(2\pi/c)$ at the center of the gap and tends to zero as the en-

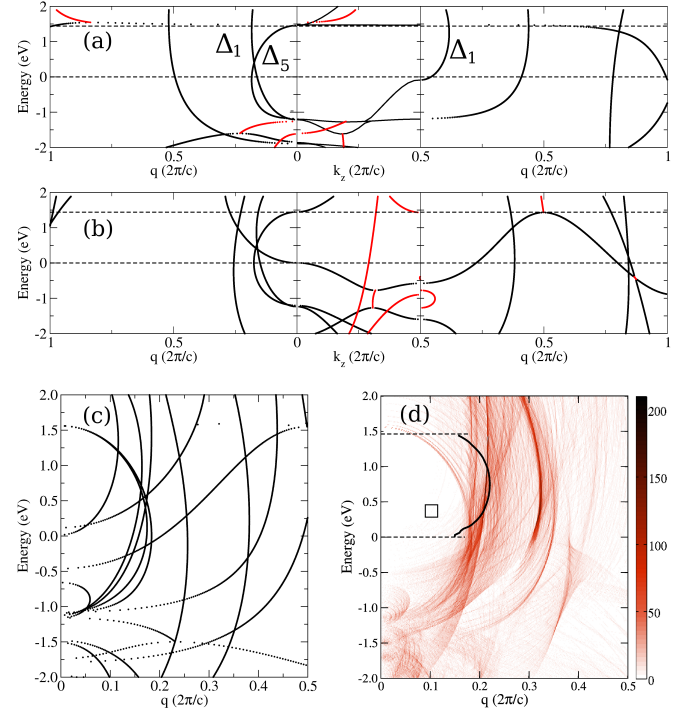


FIG. 1. (color online) Complex band structure of centrosymmetric PbTiO₃ at (a) $\mathbf{k}_{\parallel} = \bar{\Gamma}$ and (b) $\mathbf{k}_{\parallel} = \bar{X}$. Black lines at central panels correspond to bands with a real value of k_{\perp} . At left and right panels, complex bands with the form $k_{\perp} = iq$ and $k_{\perp} = \pi/c + iq$ respectively, are plotted as black lines. In red we plot complex bands with $k_z \neq 0$ or π/c , with the projections on the real plane plotted on the central panel and their projections on the imaginary plane on the side panels (following Ref. [22]). Horizontal dashed lines delimit the band gap. In (c) we plot together the imaginary part of bands with complex values of \mathbf{k} , with $\mathbf{k}_{\parallel} = \bar{\Gamma}$ or \bar{X} . (d) Density of states (in arbitrary units) with respect to the energy and the imaginary wave vector q . The density of complex bands is plotted in a red scale, where darker regions represent a larger density of bands. The black solid line represents the effective penetration length computed from the CBS (see text). The zero of energies corresponds to the top of the valence band.

ergy approaches the band edges. In Fig. 1(c) we plot together all the energy bands with associated complex values of $\mathbf{k} = (\mathbf{k}_{\parallel}, k_z + iq)$, with $\mathbf{k}_{\parallel} = \bar{\Gamma}$ or \bar{X} . Nevertheless, we have to keep in mind that the CBS at $\bar{\Gamma}$ and \bar{X} might not be representative of the whole CBS of the system, since they are only two points of special symmetry of the total 2DBZ. For a comprehensive analysis, we should gather into a plot like Fig. 1(c) the imaginary part of complex bands coming from all \mathbf{k}_{\parallel} . Instead of this, that would result into some of the infinite number of complex bands obscuring others, we plot the “density of complex bands” in Fig. 1(d). In this 2D-histogram, for every value of the energy and imaginary part of the wave vector q , we represent in a red scale the number of complex bands contributing to that $q(E)$ point. The analysis of Fig. 1(d) reveals that the total CBS is clearly domi-

nated by bands at $q \sim 0.2$ and $q \sim 0.3$. To identify the \mathbf{k}_{\parallel} that contribute to those clusters of bands we resolve the structure and, for every \mathbf{k}_{\parallel} , we plot the smallest q at a given energy [see Suppl. Fig. 3(a) in the supplemental data]. We find that from energies between the middle of the gap and the bottom of the conduction band, the most penetrating bands come from \mathbf{k}_{\parallel} lying in a narrow rectangle centered along the $\bar{\Gamma} - \bar{X}$ path, while from the top of the valence band to the center of the gap, the bands with smaller q are due to states in small circular (around $\bar{\Gamma}$) or square (around \bar{X}) regions centered at the high-symmetry points. The much larger area of the 2DBZ outside those sections contributes to the darker cluster of imaginary bands at $q \sim 0.2$. Similar results have been previously reported for other perovskites [11, 17, 23, 24]. The main messages that can be drawn might be summarized as follows: (i) the most penetrating bands (the most important for tunneling, especially in thick films) come from high-symmetry points or lines in the 2DBZ whose relative weight is small. That is the reason why those bands might be totally inappreciable in the 2D-histogram of Fig. 1(d) (see region marked with a square, where the bands with $q \sim 0.1$ at \bar{X} and $\bar{\Gamma}$ previously discussed were expected); and (ii) for ultra-thin dielectric layers or for the computation of integrated quantities (such as the interfacial dipole) it is important to consider higher order imaginary bands and non high-symmetry points in the 2DBZ, since associated phenomena might be dominated by them [25, 26].

It is sensible to think that the charge transferred from the metal to the insulator through the MIGS reflects the collective contribution of all complex band in the gap of the insulator. Here we also give a recipe to infer from the CBS an effective value of the imaginary wave vector for a given energy, $q_{\text{eff}}^{\text{CBS}}$. This can be estimated by fitting

$$\sum_{\mathbf{k}_{\parallel}} \sum_n e^{-2q_n(E, \mathbf{k}_{\parallel})z} \sim e^{-2q_{\text{eff}}^{\text{CBS}}(E)z}, \quad (1)$$

which comparison with the q_{eff} obtained from the realistic simulation of the interface is discussed below.

MIGS in first-principles simulations of capacitors. The explicit influence of the metal/ferroelectric interface in the decay of the MIGS is captured in the simulation of realistic capacitors from first-principles. Here, we have simulated short-circuited $(\text{SrRuO}_3)_m/(\text{PbTiO}_3)_n$ and $(\text{Pt})_l/(\text{PbTiO}_3)_p$ capacitors as model systems, with $m = 9.5$, $n = 8.5$, $l = 9.5$ and $p = 6.5$ unit cells, respectively. In both cases the PbTiO_3 films are terminated in a TiO_2 atomic layer, and we have checked that the band-alignment in the most stable paraelectric configuration is non-pathological [27].

The analysis of MIGS in full capacitor simulations requires to work with a spatially resolved density of states. Here, we have chosen the layer by layer projected density of states (PDOS), as defined in Eq. (21) of Ref. [27].

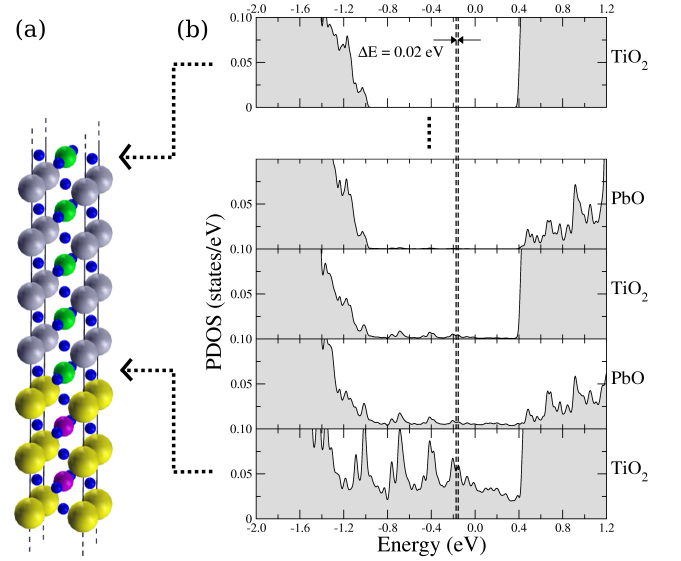


FIG. 2. (color online) (a) Schematic representation of the interface region of the simulated $(\text{SrRuO}_3)_{9.5}/(\text{PbTiO}_3)_{8.5}$ superlattice in an unpolarized configuration (Ti atoms in green, Ru in magenta, O in blue, Sr in yellow and Pb in gray). Only one of the two symmetric interfaces is shown. (b) Layer-by-layer PDOS on the atoms at the different layers, as denoted by the layer labeling. The plot at the top corresponds to the central atomic plane of the PbTiO_3 film. Dashed lines delimit one of the energy windows used to perform the integrations in Eq. (2).

The results for the $\text{SrRuO}_3/\text{PbTiO}_3$ capacitor in the unpolarized configuration are plotted in Fig. 2(b) (similar results are obtained for the Pt/PbTiO_3 interface). The decay of the evanescent tails of the MIGS can be clearly observed, with the PDOS showing a clean gap for atomic layer further than two unit cells from the interface.

We can obtain a measure of the spatial distribution of the probability density at a given energy integrating the PDOS in small windows centered at different energies inside the band gap,

$$Q_{\text{PDOS}}(E_i, z_j) = \int_{E_i - \frac{\Delta E}{2}}^{E_i + \frac{\Delta E}{2}} \rho(j, E) dE, \quad (2)$$

where $\rho(j, E)$ denotes the PDOS on all the atomic orbitals of a given layer j , located at z_j . The decay of this quantity when we move away from the interface provides a direct way to obtain the effective decay length of the PDOS, $\delta(E)$. Since δ refers to the decay of the *density*, and given the exponential behaviour of the tails of the MIGS, we can relate δ with an effective decay of the wave functions as $q_{\text{eff}}^{\text{MIGS}}(E) = 1/[2\delta(E)]$. Numerically, $\delta(E)$ is estimated first integrating the PDOS after Eq. (2) in energy windows of width $\Delta E = 0.02$ eV. Then, for every energy sampled, we plot the expo-

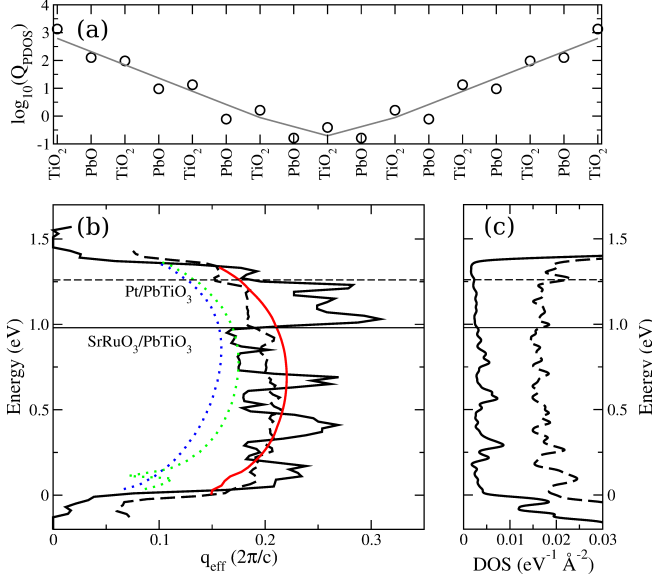


FIG. 3. (color online) (a) Decay of the MIGS for the energy window inside the gap of the SrRuO₃/PbTiO₃ capacitor shown in Fig. 2(a). The solid curve is a fit to an hyperbolic cosine, from which the effective penetration $\delta(E)$ is obtained. (b) Effective imaginary wave vector q_{eff} obtained from the CBS [using only bands at $\bar{\Gamma}$ (blue dotted line), $\bar{\Gamma}$ and \bar{X} (green dotted), and the full 2DBZ (red line)] and from the fit of the decay of the PDOS inside the insulating material for SrRuO₃/PbTiO₃ (solid black line) and Pt/PbTiO₃ capacitors (dashed black line). (c) Total DOS of MIGS in the SrRuO₃/PbTiO₃ (solid black line) and Pt/PbTiO₃ capacitors (dashed black line) obtained integrating the layer-by-layer PDOS from the interface to the center of the PbTiO₃ film. In (b) and (c) the zero of energies is set to the top of the valence band and the horizontal lines indicate the Fermi level of the corresponding capacitor.

nentially decaying Q_{PDOS} curve as a function of the distance to the interface [Fig. 3(a)], and fit it to a function $Q_{\text{PDOS}}(E, z) \simeq \cosh[z/\delta(E)]$. A hyperbolic cosine was used to account for the presence of two interfaces. Repeating this procedure for energy windows covering the whole gap we obtain the energy dependence of the effective imaginary wave vector, $q_{\text{eff}}^{\text{MIGS}}(E)$, that is plotted in Fig. 3(b) for the two different capacitors.

Comparison of decay factors obtained from bulk and interface simulations. In Fig. 3(b) we plot the effective values of the decay factors obtained from a *bulk* CBS calculation [using Eq. (1) and scaling to the band gap obtained with QUANTUM-ESPRESSO], and from the evanescent behavior of the MIGS at the interface for PbTiO₃-based capacitors with SrRuO₃ and Pt electrodes. When the full 2DBZ is used for the calculations of $q_{\text{eff}}^{\text{CBS}}$ its agreement with $q_{\text{eff}}^{\text{MIGS}}$ is very good, supporting the idea that the penetration of the MIGS is mostly determined by the bulk properties of the insulator. The correspondence is

remarkably good for the capacitor with Pt electrodes, for which a featureless dependency of $q_{\text{eff}}^{\text{MIGS}}$ with the energy is observed. For the metal oxide SrRuO₃ a more structured shape of the decay factor is noticed. In this case, to understand the peaks we have to consider interfacial effects like the symmetry filtering: the wave functions in the electrodes should match evanescent states in the insulator that are compatible by symmetry. The inspection of the bulk band structure of SrRuO₃ (see Suppl. Fig. 4 in the supplemental data) reveals the presence of a band below the Fermi energy with Δ_5 symmetry along the Γ -X line that nicely matches complex bands of PbTiO₃ of the same symmetry, with k_{\parallel} along the $\bar{\Gamma} - \bar{X}$ line of the 2DBZ. Above the Fermi energy there are no bands with the appropriate symmetry to link the complex bands with minimal q . The matching has to be done with higher order complex bands with larger q , explaining the sharp increase in $q_{\text{eff}}^{\text{MIGS}}$. In the case of Pt, there is a band with the appropriate symmetry that crosses completely the band gap of PbTiO₃. In Fig. 3(b) we also plot $q_{\text{eff}}^{\text{CBS}}$ obtained taking into account only complex bands from $\bar{\Gamma}$ and \bar{X} . As anticipated, it can be clearly noticed that only considering high symmetry points of the 2DBZ results in a severe underestimation of the effective decay factor of the MIGS.

Finally, not only the decay rate of MIGS is relevant but the interfacial DOS of MIGS is also important. We find that in this respect the two electrodes behave differently as well [see Fig. 3(c)], with Pt/PbTiO₃ capacitor showing a much larger surface density of MIGS than the SrRuO₃/PbTiO₃ one. This is consistent with the much larger DOS in the vicinity of the Fermi level of bulk Pt with respect to SrRuO₃.

Influence of the ferroelectric polarization. The influence of the ferroelectric distortion in the spatial and energetic distribution of the evanescent states is known to play a mayor role on the electro [17, 23, 28] and magnetoresistance [11, 13, 29] of ferroelectric tunnel junctions. Unfortunately, a thorough analysis of such effect using the arguments developed in this work is limited by band alignment issues [27] that restrict the possible electrodes and the magnitude of the polarization that can be explored. In our case, only the ferroelectric capacitor with SrRuO₃ electrodes and $n = 8.5$ is non-pathological [27], with a polarization within PbTiO₃ of $24 \mu\text{C}/\text{cm}^2$. Again, the agreement between $q_{\text{eff}}^{\text{MIGS}}$ (see Supplemental data for details about how to compute $q_{\text{eff}}^{\text{MIGS}}$ in the polar state) and $q_{\text{eff}}^{\text{CBS}}$ (computed from the CBS of bulk PbTiO₃ at the same polarization as in the capacitor) is very good (see Suppl. Fig. 5 in the supplemental data). A general increase of the effective decay factor (i.e. shorter penetration lengths) with the polarization is observed. This growth of q is due to two different factors. First, the polarization opens the gap. Second, it pushes up the flat band along the Γ -X line at the bottom of the conduction band in the paraelectric configuration (see Suppl.

Fig. 6 in the supplemental data). Both facts increase the imaginary part of those bands that link to the bottom of the conduction band with \mathbf{k}_{\parallel} along the $\bar{\Gamma} - \bar{X}$ line. This effect has already been reported for the complex bands at $\bar{\Gamma}$ in BaTiO_3 [17, 29], and was invoked to explain the impact of ferroelectricity in the tunnel conductivity of ferroelectric junctions.

Summary. The main conclusions that can be drawn from this work are: (i) although the most penetrating bands are located at high-symmetry points, for the study of tunneling across ultra-thin layers or integrated quantities (where many \mathbf{k}_{\parallel} contribute) it is important to consider complex bands in the whole 2DBZ; (ii) we have given a general recipe to estimate from the CBS of the bulk insulator the effective decay factor (and its dependence with the energy within the gap) of the MIGS in realistic interfaces, showing a very good agreement with the results obtained from first-principles simulations of capacitors; (iii) to explain the fine details, especially when metal-oxide electrodes are used, a symmetry filtering analysis has to be performed; and (iv) the ferroelectric polarization can be used as a knob to increase the decay factor of the CBS. The accuracy of the model used to predict the effective decay length of MIGS would allow to screen materials to be used as barriers in tunnel electro- and magnetoresistance junctions based on knowledge. We hope this work will encourage experiments and set the ground for future theoretical studies of MIGS, tunneling and related phenomena.

The authors thank K. M. Rabe and M. H. Cohen for helpful discussion. This work was supported by the Spanish Ministry of Science and Innovation through the MICINN Grant FIS2009-12721-C04-02, by the Spanish Ministry of Education through the FPU fellowship AP2006-02958 (PAP), and by the European Union through the project EC-FP7, Grant No. CP-FP 228989-2 “OxIDES”. The authors thankfully acknowledge the computer resources, technical expertise and assistance provided by the Red Española de Supercomputación. Calculations were also performed at the ATC group of the University of Cantabria.

[1] P. Zubko, S. Gariglio, M. Gabay, Ph. Ghosez and J.-M. Triscone, *Annu. Rev. Condens. Matter Phys.*, **2**, 141 (2011).
 [2] V. Heine, *Phys. Rev.*, **138**, A1689 (1965).
 [3] R. T. Tung, *Mater. Sci. Eng. Rep.*, **35**, 1 (2001) and references therein..
 [4] A. A. Demkov, L. R. C. Fonseca, E. Verret, J. Tomfohr and O. F. Sankey, *Phys. Rev. B*, **71**, 195306 (2005).
 [5] M. Y. Zhuravlev, R. F. Sabirianov, S. S. Jaswal and E. Y. Tsymbal, *Phys. Rev. Lett.*, **94**, 246802 (2005).

[6] E. Y. Tsymbal and H. Kohlstedt, *Science*, **313**, 181 (2006).
 [7] A. Gruverman, D. Wu, H. Lu, Y. Wang, H. W. Jang, C. M. Folkman, M. Y. Zhuravlev, D. Felker, M. Rzechowski, C. B. Eom and E. Y. Tsymbal, (2009).
 [8] P. Maksymovych, S. Jesse, P. Yu, R. Ramesh, A. P. Badorf and S. V. Kalinin, *Science*, **324**, 1421 (2009).
 [9] V. García, S. Fusil, K. Bouzehouane, S. Enouz-Vedrenne, N. D. Mathur, A. Barthélémy and M. Bibes, *Nature*, **460**, 81 (2009).
 [10] J. D. Burton and E. Y. Tsymbal, *Phys. Rev. Lett.*, **106**, 157203 (2011).
 [11] J. P. Velev, K. D. Belashchenko, D. A. Stewart, M. van Schilfgaarde, S. S. Jaswal and E. Y. Tsymbal, *Phys. Rev. Lett.*, **95**, 216601 (2005).
 [12] V. Garcia, M. Bibes, L. Bocher, S. Valencia, F. Kronast, A. Crassous, X. Moya, S. Enouz-Vedrenne, A. Gloter, D. Imhoff, C. Deranlot, N. D. Mathur, S. Fusil, K. Bouzehouane and A. Barthélémy, *Science*, **327**, 1106 (2010).
 [13] N. M. Caffrey, T. Archer, I. Rungger and S. Sanvito, *Phys. Rev. Lett.*, **109**, 226803 (2012).
 [14] A. Zangwill, *Physics at Surfaces* (Cambridge University Press, Cambridge, 1988).
 [15] M. Bibes, J. E. Villegas and A. Barthélémy, *Advances in Physics*, **60**, 5 (2012).
 [16] K. Janicka, J. P. Velev and E. Y. Tsymbal, *Phys. Rev. Lett.*, **102**, 106803 (2009).
 [17] J. P. Velev, C.-G. Duan, K. D. Belashchenko, S. S. Jaswal and E. Y. Tsymbal, *Phys. Rev. Lett.*, **98**, 137201 (2007).
 [18] J. K. Tomfohr and O. F. Sankey, *Phys. Rev. B*, **65**, 245105 (2002).
 [19] J. M. Soler, E. Artacho, J. D. Gale, A. García, J. Junquera, P. Ordejón and D. Sánchez-Portal, *J. Phys.: Condens. Matter*, **14**, 2745 (2002).
 [20] P. Giannozzi, S. Baroni, N. Bonini, M. Calandra, R. Car, C. Cavazzoni, D. Ceresoli, G. L. Chiarotti, M. Cococcioni, I. Dabo, A. D. Corso, S. de Gironcoli, S. Fabris, G. Fratesi, R. Gebauer, U. Gerstmann, C. Gougoussis, A. Kokalj, M. Lazzeri, L. Martin-Samos, N. Marzari, F. Mauri, R. Mazzarello, S. Paolini, A. Pasquarello, L. Paulatto, C. Sbraccia, S. Scandolo, G. Sciauzero, A. P. Seitsonen, A. Smogunov, P. Umari and R. M. Wentzcovitch, *J. Phys.: Condens. Matter*, **21**, 395502 (2009).
 [21] A. Smogunov, A. DalCorso and E. Tosatti, *Phys. Rev. B*, **70**, 045417 (2004).
 [22] Y. C. Chang, *Phys. Rev. B*, **25**, 605 (1982).
 [23] N. F. Hinsche, M. Fechner, P. Bose, S. Ostanin, J. Henk, I. Mertig and P. Zahn, *Phys. Rev. B*, **82**, 214110 (2010).
 [24] D. Wortmann and S. Blügel, *Phys. Rev. B*, **83**, 155114 (2011).
 [25] P. Mavropoulos, N. Papanikolaou and P. H. Dederichs, *Phys. Rev. Lett.*, **85**, 1088 (2000).
 [26] W. H. Butler, X. G. Zhang, T. C. Schulthess and J. M. MacLaren, *Phys. Rev. B*, **63**, 054416 (2001).
 [27] M. Stengel, P. Aguado-Puente, N. A. Spaldin and J. Junquera, *Phys. Rev. B*, **83**, 235112 (2011).
 [28] N. M. Caffrey, T. Archer, I. Rungger and S. Sanvito, *Phys. Rev. B*, **83**, 125409 (2011).
 [29] J. P. Velev, C. G. Duan, J. D. Burton, A. Smogunov, M. K. Niranjana, E. Tosatti, S. S. Jaswal and E. Y. Tsymbal, *Nano Letters*, **9**, 427 (2009).

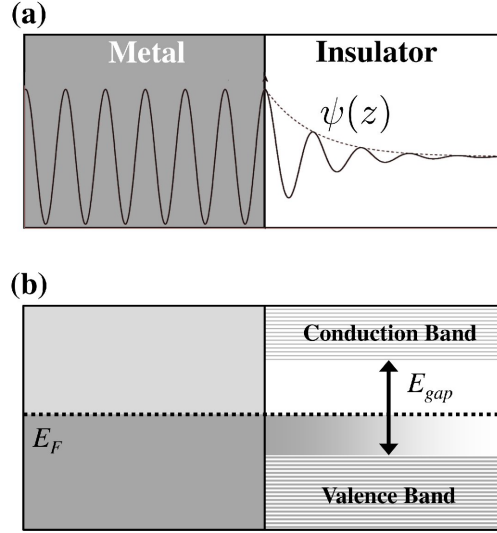
First-principles study of metal-induced gap states in metal/oxide interfaces and their relation with the complex band structure. Supplemental Material

Pablo Aguado-Puente¹ and Javier Junquera¹

¹*Departamento de Ciencias de la Tierra y Física de la Materia Condensada,
Universidad de Cantabria, Cantabria Campus Internacional,
Avenida de los Castros s/n, 39005 Santander, Spain*

(Dated: January 13, 2014)

I. SCHEMATIC REPRESENTATION OF METAL-INDUCED GAP STATES (MIGS).



Suppl. FIG. 1. Schematic representation of metal-induced gaps states in a metal/insulator interface. In (a), the wave function of an electronic state with an eigenvalue within the insulator band gap takes the form of a propagating wave function in the metallic side that decays exponentially on the insulating side. A schematic representation of the band alignment of the interface is shown in (b). MIGS below the Fermi level of the junction are populated and the resulting injection of charge is an important contribution to the interfacial dipole that determines the band alignment.

II. COMPUTATIONAL DETAILS.

Simulations on this work have been performed within the local density approximation (LDA) in the Ceperley-Alder parametrization¹ as implemented in two different codes: SIESTA^{2,3} for the simulation of realistic capacitors, and the QUANTUM-ESPRESSO^{4,5} package for the complex band structure calculations.⁶ The use of two different codes is a delicate issue and thus keeping strict convergence criteria becomes critical in order to ensure the compatibility of all the simulations.

In order to simulate the effect of the mechanical boundary conditions due to the strain imposed by the substrate, in all the simulations the in-plane lattice constant was fixed to the theoretical equilibrium lattice constant of bulk SrTiO₃ ($a = 3.85$ Å for QUANTUM-ESPRESSO and $a = 3.874$ Å for SIESTA). Since SrRuO₃ is paraelectric at room temperature, we have assumed non-spin polarized configurations.

During the structural optimizations of both bulk PbTiO₃ and the capacitors, a Monkhorst-Pack^{7,8} mesh equivalent to $12 \times 12 \times 12$ in a perovskite unit cell was used for the sampling of the reciprocal space. Tolerances for the forces and stresses were 0.01 eV/Å and 0.0001 eV/Å³, respectively. Other computational parameters, specific to each code, are summarized below.

A. QUANTUM-ESPRESSO

Complex band structure of bulk PbTiO_3 has been calculated using a density-functional plane-wave code with pseudopotentials. We have used the ultrasoft Vanderbilt pseudopotentials tabulated in the Vanderbilt Ultra-Soft Pseudopotential Site.⁹ The plane-wave cutoff was set to 40 Ry. For the generation of the 2D-histogram of Fig. 1(d) of the main body of the manuscript, a 48×48 mesh of \mathbf{k}_{\parallel} points over the two-dimensional Brillouin zone (2DBZ) was sampled.

B. SIESTA

Computations on short-circuited Pt/PbTiO_3 and $\text{SrRuO}_3/\text{PbTiO}_3$ capacitors were performed using a numerical atomic orbital method, as implemented in the SIESTA code.² Core electrons were replaced by fully-separable¹⁰ norm-conserving pseudopotentials, generated following the recipe given by Troullier and Martins.¹¹ Further details on the pseudopotentials and basis sets can be found in Ref. 12.

A Fermi-Dirac distribution was chosen for the occupation of the one-particle Kohn-Sham electronic eigenstates, with a smearing temperature of 8 meV (100 K). The electronic density, Hartree, and exchange-correlation potentials, as well as the corresponding matrix elements between the basis orbitals, were computed on a uniform real space grid, with an equivalent plane-wave cutoff of 1200 Ry in the representation of the charge density.

The capacitors were simulated by using a supercell approximation with periodic boundary conditions.¹³ A (1×1) periodicity of the supercell perpendicular to the interface is assumed. This inhibits the appearance of ferroelectric domains and/or tiltings and rotations of the O octahedra. A reference ionic configuration was defined by piling up a number of unit cells of the perovskite oxide (8.5 for the SrRuO_3 -based capacitor and 6.5 for the Pt-based capacitor), and 9.5 unit cells of the metal electrode. The PbTiO_3 films are always terminated in a TiO_2 atomic layer.

To simulate the capacitors in a non polar configuration, we imposed a mirror symmetry plane at the central TiO_2 layer, and relaxed the resulting tetragonal supercells within $P4/mmm$ symmetry. For the ferroelectric capacitors a second minimization was carried out, with the constraint of the mirror symmetry plane lifted. We have checked that the band-alignment in all systems reported here is non-pathological.¹⁴

III. BULK BAND STRUCTURE OF PbTiO_3 .

We compare complex band structure calculations on bulk PbTiO_3 with properties of MIGS in capacitors where the out-of-plane cell vectors were allowed to relax. As required by the strong sensitivity of complex bands on the real band structure, bulk calculations must be performed under the same symmetry constraints applied to the PbTiO_3 layer in the capacitor. It is important to note here that the bulk paraelectric phase discussed in this work is not the cubic phase, but a tetragonal centrosymmetric $P4/mmm$ phase. The in-plane lattice constant was fixed to the theoretical one of SrTiO_3 and the out-of-plane stress was relaxed while the atomic positions were kept in the centrosymmetric positions.

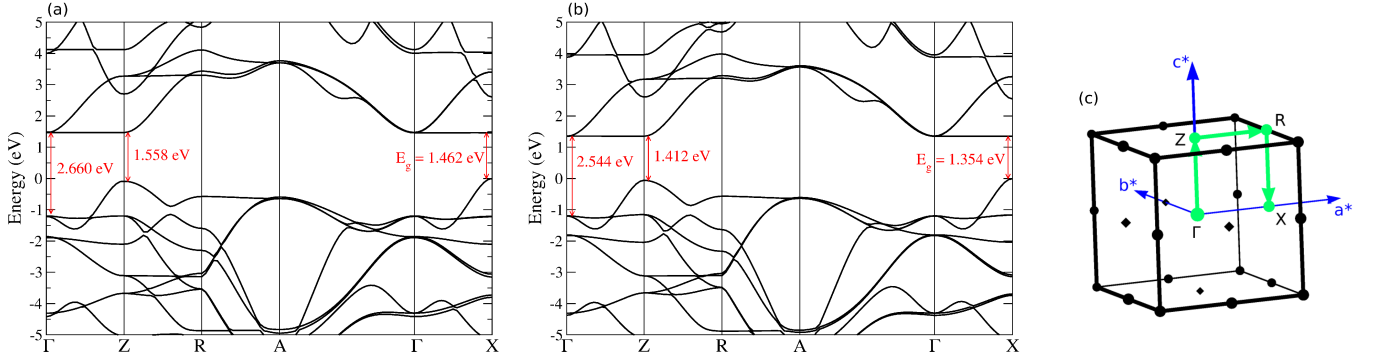
Given the sensitivity of complex bands to the size of the gap and the curvature of real bands they connect with,¹⁵ a good agreement between the band structures obtained with both codes is required to obtain comparable results. Suppl. Fig. 2 shows that the band structures calculated with the two different codes are virtually identical in shape, although the QUANTUM-ESPRESSO calculation displays a slightly larger gap. This must be taken into account since, in principle, a larger gap should translate into slightly larger values of the imaginary part of the complex wave vectors.

IV. DETAILS ON THE ANALYSIS OF MIGS IN FIRST-PRINCIPLES SIMULATIONS OF CAPACITORS.

The analysis of MIGS in full capacitor simulations requires to work with some sort of energy-resolved probability density. For this, a spatially resolved density of states is defined as

$$\rho(i, E) = \sum_n \int_{\text{BZ}} d\mathbf{k} |\langle i | \psi_{n\mathbf{k}} \rangle|^2 \delta(E - E_{n\mathbf{k}}), \quad (1)$$

where $|i\rangle$ is a normalized function, localized in space around the region of interest.



Suppl. FIG. 2. (color online) Band structures of bulk non-polar PbTiO_3 obtained with (a) QUANTUM-ESPRESSO and (b) SIESTA. A direct gap is found at X. (c) Schematic of the Brillouin zone in a simple tetragonal lattice.

When $|i\rangle = |\mathbf{r}\rangle$ is an eigenstate of the position operator, the resulting $\rho(\mathbf{r}, E)$ is commonly known as *local density of states*. However, strong oscillations of this function due to the underlying atomic structure difficult the analysis. Alternatively, the nanosmoothed version of this function might be used, but some interfacial properties, like precisely the decay length of the MIGS charge in the band gap, are sensitive to the specific convolution function used for the nanosmoothing procedure.¹⁶

A reasonable choice is to work with the layer-by-layer (z -resolved) PDOS (E -resolved), defined as in Eq. (1) where $|i\rangle = |\phi_{nlm}\rangle$ is an atomic orbital of specified quantum numbers (n, l, m) . In this case the bias of the method lies in the choice of the basis of atomic orbitals. A sufficiently converged basis should minimize its effect since atoms of the same species at different sites are equally described, so the z dependence might be considered as less biased than with previous methods. In Fig. 2 of the main body of the manuscript we plot the layer-by-layer PDOS corresponding to the $\text{PbTiO}_3/\text{SrRuO}_3$ capacitor.

The energy distribution of the charge density converges much slower with the k -point sampling than its spatial distribution. For this reason the PDOS was calculated performing an extra non-self consistent calculation with a finer k -point grid of $54 \times 54 \times 9$.

V. SYMMETRY FILTERING AT THE $\text{PbTiO}_3/\text{SrRuO}_3$ INTERFACE

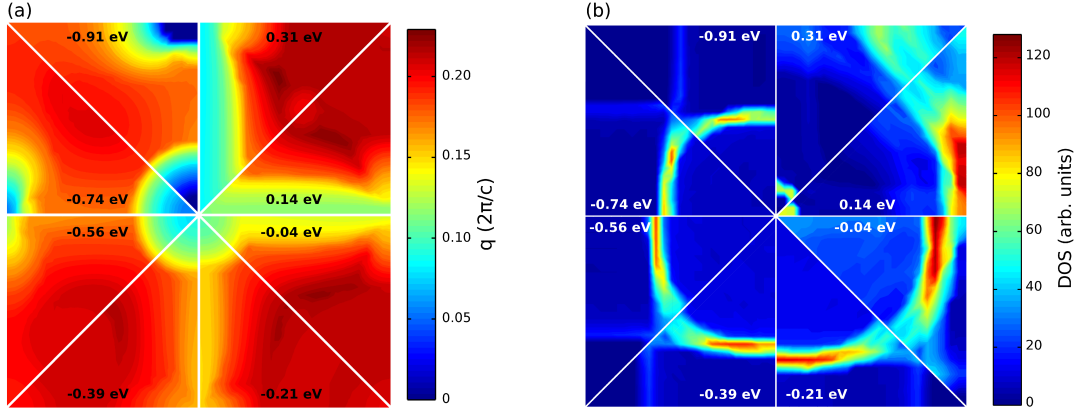
Fig. 3(b) of the main body of the text of this work reveals some differences in the properties of MIGS of capacitors with SrRuO_3 or Pt electrodes. The dependence of the effective decay factor with the energy is essentially featureless in the case of Pt electrodes, while for SrRuO_3 this curve presents some structure. The most remarkable characteristic in the latter case is a sharp increase in the effective imaginary wave vector in the uppermost part of the PbTiO_3 gap, right above the Fermi level of the capacitor. This behavior is not due to intrinsic characteristics of the complex band structure of PbTiO_3 but to the interface.

The interface affects the energy dependence of the MIGS penetration mainly through the symmetry filtering: wave functions in the electrodes should match evanescent states in the insulator that are compatible by symmetry, filtering the complex bands that contribute to the effective value.

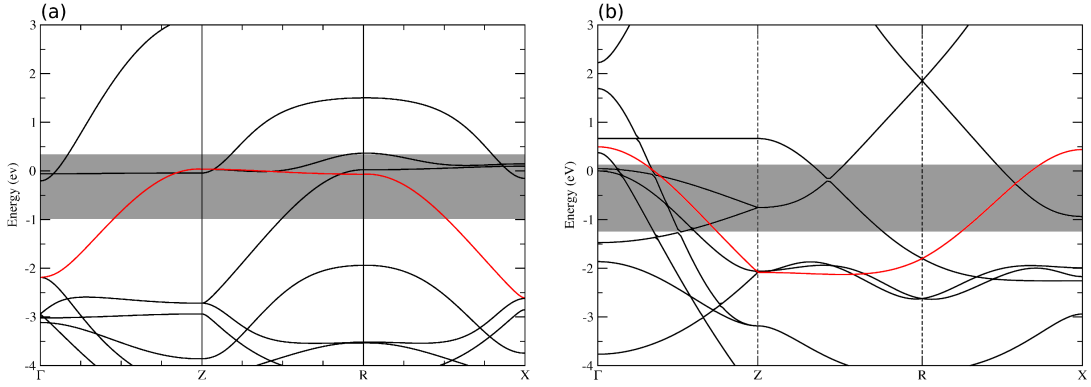
In Suppl. Fig. 3(a) we plot the complex band of minimum q for paraelectric PbTiO_3 over the 2DBZ. We find that from the top of the valence band to the center of the gap, the bands with smaller q are due to states in small circular (around $\bar{\Gamma}$) or square (around \bar{X}) regions centered at the high-symmetry points, while from energies between the middle of the gap and the bottom of the conduction band, the most penetrating bands come from \mathbf{k}_{\parallel} lying in a narrow rectangle centered along the $\bar{\Gamma} - \bar{X}$ path. As can be seen in Fig. 1 of the main body of the manuscript, these deep-penetrating bands along the high symmetry $\bar{\Gamma} - \bar{X}$ line are those that link to the bottom of the conduction band and have Δ_5 symmetry at the $\bar{\Gamma}$ point.

The symmetry analysis of the band structure of bulk SrRuO_3 , depicted in Suppl. Fig. 4(a), reveals that there is a band (highlighted in red) with the same symmetry as the evanescent states discussed above all along the $\bar{\Gamma} - \bar{X}$ line, and that has its maximum around the Fermi level. For higher energies there are no bands with the appropriate symmetry to link the complex bands of minimal q and form deep-penetrating MIGS. The matching has to be done with higher order complex bands with larger q . This explains the sharp increase of the effective imaginary part of the wave vector for energies above the Fermi level obtained in the $\text{PbTiO}_3/\text{SrRuO}_3$ capacitor.

For Pt there is a band with the appropriate Δ_5 symmetry that crosses completely the band gap, as shown in Suppl.



Suppl. FIG. 3. (color online) (a) Minimum value of the imaginary part of the complex wave vector (maximum penetration) for bulk paraelectric PbTiO₃ over the 2DBZ. (b) DOS of SrRuO₃ over the 2DBZ. Both quantities are shown for eight different values of the energy, referred to the Fermi level of the PbTiO₃/SrRuO₃ capacitor. The center of each panel represents the $\bar{\Gamma}$ point, while the centers of each side symbolizes the \bar{X} point.



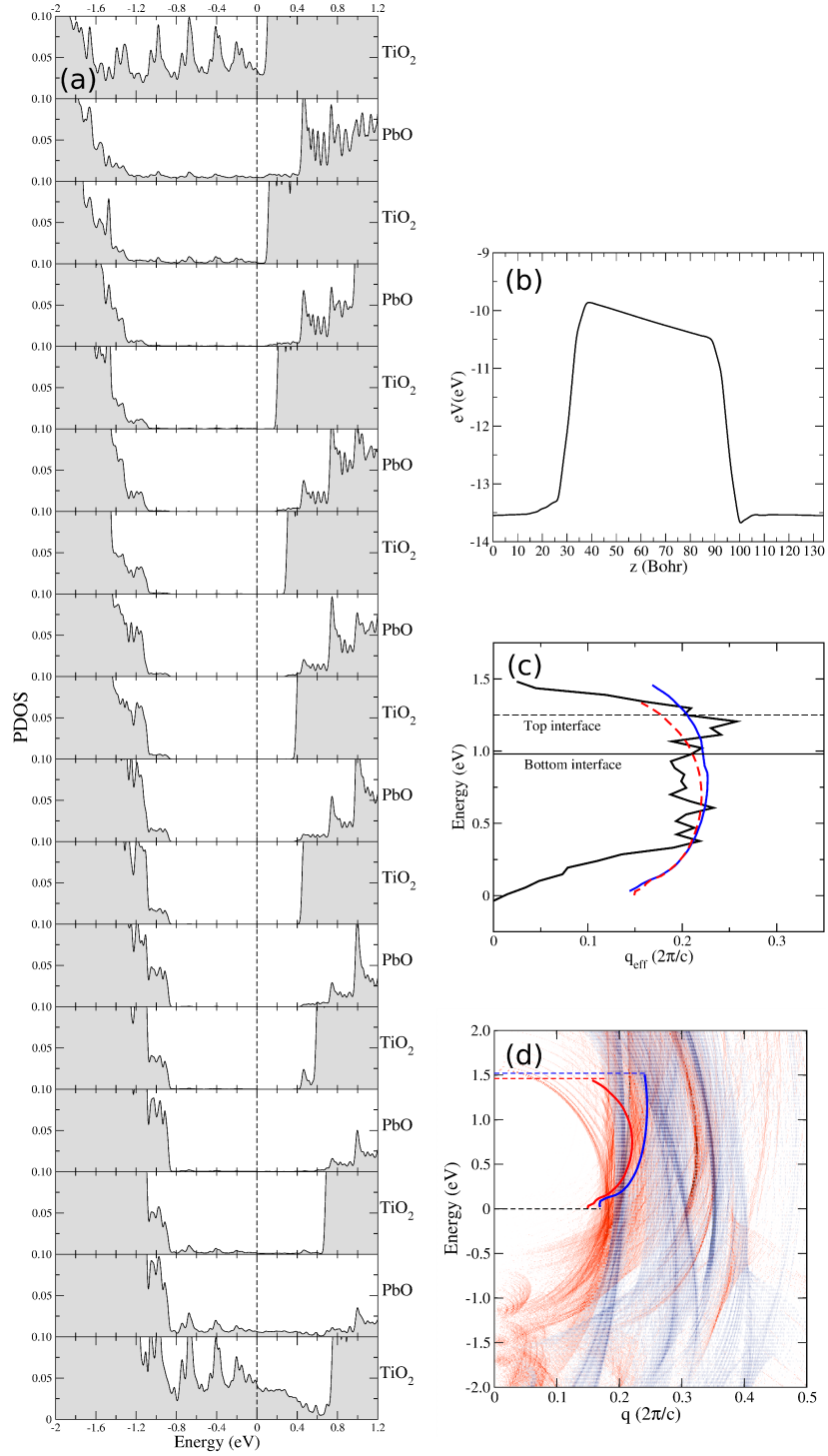
Suppl. FIG. 4. (color online) Bulk real band structure of (a) bulk SrRuO₃ and (b) bulk Pt along the relevant directions in the 3-D Brillouin zone of the $P4/mmm$ tetragonal phase. The bands highlighted in red has symmetry Δ_5 along the $\bar{\Gamma}$ -X line, and match complex bands in the PbTiO₃ with the same symmetry with \mathbf{k}_{\parallel} along the line $\bar{\Gamma} - \bar{X}$. The gray area indicates the band gap alignment of the PbTiO₃ layer for the corresponding capacitors.

Fig. 4(b). In other words, all the complex bands with minimum q along the $\bar{\Gamma} - \bar{X}$ path find a symmetry-compatible band in the Pt electrode to link with, explaining the featureless shape of $q_{\text{eff}}^{\text{MIGS}}$.

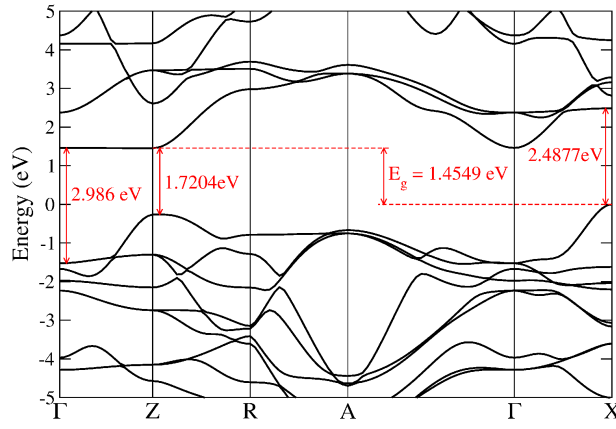
Other interface-intrinsic mechanism that could affect the energy dependence of the $q_{\text{eff}}^{\text{MIGS}}$ is the \mathbf{k}_{\parallel} -dependence of the DOS of the metal. For instance, for a given energy, a DOS concentrated away from the high symmetry points $\bar{\Gamma}$ and \bar{X} , or the high symmetry path $\bar{\Gamma} - \bar{X}$ [where the most penetrating complex bands are found, see Suppl. Fig. 3(a)] would cause an increase of $q_{\text{eff}}^{\text{MIGS}}$ at that particular energy. This mechanism does not seem to contribute to the sudden increase of $q_{\text{eff}}^{\text{MIGS}}$ at the Fermi level in the SrRuO₃/PbTiO₃ capacitor: the DOS of SrRuO₃ varies smoothly with the energy and has a significant density around the high symmetry points and paths near the Fermi level [see Fig. 3(b)].

VI. DISCUSSION ABOUT THE EFFECT OF THE FERROELECTRIC POLARIZATION OF THE PbTiO₃ LAYER

Most of the discussions in the main text of the manuscript regard the paraelectric phase of the PbTiO₃/SrRuO₃ capacitor. However, PbTiO₃ is a ferroelectric perovskite with a large spontaneous polarization in bulk¹⁷. Indeed, the influence of the polarization in the spatial and energetic distribution of evanescent states in ferroelectric/metal interfaces has been proposed to contribute largely to the electro-^{18–20} and magnetoresistance^{21–23} of ferroelectric



Suppl. FIG. 5. (color online) (a) Layer-by-layer PDOS of a polar $[\text{SrRuO}_3]_{9.5}/[\text{PbTiO}_3]_{8.5}$ capacitor. The dashed line indicates the Fermi level. (b) Profile of the macroscopically-averaged electrostatic potential across the capacitor. (c) Effective imaginary wave vectors obtained from the fit of the decay of the PDOS of the PbTiO_3 layer in the polar capacitor (black line), from the CBS of bulk PbTiO_3 with the same ferroelectric distortion as in the center of the capacitor (blue line) and from the CBS of centrosymmetric PbTiO_3 (red line). The two horizontal lines indicate the position of the Fermi level at the two interfaces (note that in the capacitor the Fermi level is the same across the whole structure, but to extract $q_{\text{eff}}^{\text{MIGS}}(E)$ the PDOS at each atomic layer is shifted following the electrostatic potential to align the band structures). (d) Complex band structure of centrosymmetric $P4/mmm$ (red) and fully relaxed ferroelectric (blue) PbTiO_3 . The plot was obtained following the same recipe as for Fig. 1(d) of the main manuscript. Red and blue solid lines are the effective decays obtained from the CBS of centrosymmetric and polarized PbTiO_3 respectively. Red and blue dashed lines correspond to the bottom of the conduction band in each case. The zero of energies in panels (c) and (d) is set to the top of the valence band.



Suppl. FIG. 6. (color online) Band structure of bulk ferroelectric PbTiO₃ with the in-plane lattice constant fixed to the theoretical one of SrTiO₃. Band structure calculated with SIESTA.

tunnel junctions. A thorough analysis of such effect, using similar arguments as those developed in this paper, would be very useful in this regard. It should be noted, however, that the investigation of those aspects related with the realistic interfaces has the limitation imposed by the band alignment issues reported elsewhere¹⁴, that restrict (i) the number of possible electrodes that can be tested within the usual approximations to the exchange-correlation functional (only for SrRuO₃, a sizable polarization can be induced in the PbTiO₃ layer before causing the spurious electric breakdown of the capacitor) and (ii) the magnitude of the polarization (even for SrRuO₃ electrodes, the interface becomes pathological for polarizations of the PbTiO₃ layer larger than $\sim 40 \mu\text{C}/\text{cm}^2$).

For the capacitors discussed here, we find only the [SrRuO₃]_{9.5}/[PbTiO₃]_{8.5} capacitor to display a correct band alignment in the polar configuration, with a polarization of $24 \mu\text{C}/\text{cm}^2$ after relaxing under short-circuit boundary conditions. Suppl. Fig. 5(a) displays the layer-by-layer PDOS in the PbTiO₃ film. The tilting of the bands due to the remnant depolarizing field is clearly appreciable. To extract the $q_{\text{eff}}^{\text{MIGS}}$ from the PDOS using the same recipe developed in the main manuscript we have to take into account that here the band structure at different atomic layers is shifted as a result of the depolarizing field. To perform the fitting of the decay of the MIGS in the same fashion as in Fig. 3(a) of the main paper, we align the layer-by-layer PDOS using the macroscopic average of the electrostatic potential, shown in Suppl. Fig. 5(b). The resulting $q_{\text{eff}}^{\text{MIGS}}(E)$ for the ferroelectric configuration of the SrRuO₃/PbTiO₃ capacitor is shown as a black line in Suppl. Fig. 5(c). When compared with the $q_{\text{eff}}^{\text{CBS}}(E)$ obtained for bulk PbTiO₃ with the same ferroelectric distortion a good agreement is found, as in the paraelectric configuration. For such polarization ($24 \mu\text{C}/\text{cm}^2$) the change in the effective decay of MIGS induced by the ferroelectric distortion is not very large.

To appreciate better the effect of the ferroelectricity in the MIGS we compute the CBS for the fully relaxed bulk PbTiO₃ (which displays a polarization of $81 \mu\text{C}/\text{cm}^2$ when the in-plane lattice constant is fixed to that of SrTiO₃). The resulting $q_{\text{eff}}^{\text{CBS}}$ is plotted in Suppl. Fig. 5(d).

The effect of the ferroelectric distortion on the band structure of PbTiO₃ is two-folded (see Suppl. Fig. 6). In first place it opens the gap, tending to increase the imaginary part of the complex bands wave vectors. In addition, it pushes up the flat band that constitutes the bottom of the conduction band along the Γ -X path in the paraelectric configuration. Suppl Fig. 5(d) shows that this increases greatly the imaginary part of those bands that link to the bottom of the conduction band with k_{\parallel} along the $\bar{\Gamma} - \bar{X}$. Suppl. Fig. 5(d) also shows that, while complex bands at high symmetry paths of the 2DBZ are indeed strongly affected by the polarization of PbTiO₃, the dense cluster of bands with $q \sim 0.2$ ($2\pi/c$) display very little distortion in the polar state with respect to the non-polar one. The net result is a decrease of the penetration of MIGS, that is larger the closer the energy is to the conduction band, as evidenced by the estimated $q_{\text{eff}}^{\text{CBS}}$ shown in Suppl Fig. 5(d).

¹ D. M. Ceperley and B. J. Alder, Phys. Rev. Lett., **45**, 566 (1980).

² J. M. Soler, E. Artacho, J. D. Gale, A. García, J. Junquera, P. Ordejón, and D. Sánchez-Portal, J. Phys.: Condens. Matter, **14**, 2745 (2002).

³ See the SIESTA web page: <http://www.icmab.es/siesta>.

- ⁴ P. Giannozzi, S. Baroni, N. Bonini, M. Calandra, R. Car, C. Cavazzoni, D. Ceresoli, G. L. Chiarotti, M. Cococcioni, I. Dabo, A. D. Corso, S. de Gironcoli, S. Fabris, G. Fratesi, R. Gebauer, U. Gerstmann, C. Gougoussis, A. Kokalj, M. Lazzeri, L. Martin-Samos, N. Marzari, F. Mauri, R. Mazzarello, S. Paolini, A. Pasquarello, L. Paulatto, C. Sbraccia, S. Scandolo, G. Schlauser, A. P. Seitsonen, A. Smogunov, P. Umari, and R. M. Wentzcovitch, *J. Phys.: Condens. Matter*, **21**, 395502 (2009).
- ⁵ See the QUANTUM-ESPRESSO web page: <http://www.quantum-espresso.org>.
- ⁶ A. Smogunov, A. D. Corso, and E. Tosatti, *Phys. Rev. B*, **70**, 045417 (2004).
- ⁷ H. J. Monkhorst and J. D. Pack, *Phys. Rev. B*, **13**, 5188 (1976).
- ⁸ J. Moreno and J. M. Soler, *Phys. Rev. B*, **45**, 13891 (1992).
- ⁹ See <http://www.physics.rutgers.edu/~dhv/uspp/>.
- ¹⁰ L. Kleinman and D. M. Bylander, *Phys. Rev. Lett.*, **48**, 1425 (1982).
- ¹¹ N. Troullier and J. L. Martins, *Phys. Rev. B*, **43**, 1993 (1991).
- ¹² J. Junquera, M. Zimmer, P. Ordejón, and Ph. Ghosez, *Phys. Rev. B*, **67**, 155327 (2003).
- ¹³ M. Payne, M. Teter, D. Allan, T. Arias, and J. Joannopoulos, *Rev. Mod. Phys.*, **64**, 1045 (1992).
- ¹⁴ M. Stengel, P. Aguado-Puente, N. A. Spaldin, and J. Junquera, *Phys. Rev. B*, **83**, 235112 (2011).
- ¹⁵ Y. C. Chang, *Phys. Rev. B*, **25**, 605 (1982).
- ¹⁶ J. Junquera, M. H. Cohen, and K. M. Rabe, *J. Phys.: Condens. Matter*, **19**, 213203 (2007).
- ¹⁷ W. Zhong, R. D. King-Smith, and D. Vanderbilt, *Phys. Rev. Lett.*, **72**, 3618 (1994).
- ¹⁸ J. P. Velev, C.-G. Duan, K. D. Belashchenko, S. S. Jaswal, and E. Y. Tsymbal, *Phys. Rev. Lett.*, **98**, 137201 (2007).
- ¹⁹ N. F. Hinsche, M. Fechner, P. Bose, S. Ostanin, J. Henk, I. Mertig, and P. Zahn, *Phys. Rev. B*, **82**, 214110 (2010).
- ²⁰ N. M. Caffrey, T. Archer, I. Rungger, and S. Sanvito, *Phys. Rev. B*, **83**, 125409 (2011).
- ²¹ J. P. Velev, K. D. Belashchenko, D. A. Stewart, M. van Schilfgaarde, S. S. Jaswal, and E. Y. Tsymbal, *Phys. Rev. Lett.*, **95**, 216601 (2005).
- ²² J. P. Velev, C. G. Duan, J. D. Burton, A. Smogunov, M. K. Niranjana, E. Tosatti, S. S. Jaswal, and E. Y. Tsymbal, *Nano Letters*, **9**, 427 (2009).
- ²³ N. M. Caffrey, T. Archer, I. Rungger, and S. Sanvito, *Phys. Rev. Lett.*, **109**, 226803 (2012).